

# We are IntechOpen, the world's leading publisher of Open Access books Built by scientists, for scientists

6,900

Open access books available

185,000

International authors and editors

200M

Downloads

Our authors are among the

154

Countries delivered to

TOP 1%

most cited scientists

12.2%

Contributors from top 500 universities



WEB OF SCIENCE™

Selection of our books indexed in the Book Citation Index  
in Web of Science™ Core Collection (BKCI)

Interested in publishing with us?  
Contact [book.department@intechopen.com](mailto:book.department@intechopen.com)

Numbers displayed above are based on latest data collected.  
For more information visit [www.intechopen.com](http://www.intechopen.com)



---

# Computational Fluid Dynamics of Blood Flow in the Abdominal Aorta Post “Chimney” Endovascular Aneurysm Repair (ChEVAR)

---

Hila Ben Gur, Moses Brand, Gábor Kósa and Saar Golan

Additional information is available at the end of the chapter

<http://dx.doi.org/10.5772/64611>

---

## Abstract

Abdominal aortic aneurysms (AAAs) are a significant cause of death in the Western world. Endovascular aneurysm repair (EVAR) is becoming the prevalently used procedure to repair AAAs (versus the traditional approach of open surgery). In cases of infrarenal AAAs, there is a risk of the renal arteries being blocked by the stent graft (SG) inserted to repair the aneurysm. In these cases, two additional SGs termed “chimney” stent grafts (CSGs) are inserted into the renal arteries in parallel with the main SG to exclude this hazard. In this study, the hemodynamics of an infrarenal AAA endovascularly repaired by a system of SGs using the “chimney” technique is investigated. Two AAA models are analyzed using computational fluid dynamics (CFD, Ansys Fluent)—a healthy abdominal aorta and an abdominal aorta post “chimney” endovascular aneurysm repair (ChEVAR) with a CSG inserted into each renal artery in parallel with the aortic SG. Results indicate that CSGs induce stagnation zones downstream the renal arteries yet mild and confined overall flow and wall shear stress (WSS) modifications. The flow regime remains principally laminar. The study findings indicate the limited hemodynamic modifications of the ChEVAR procedure and thus further support its merit.

**Keywords:** abdominal aortic aneurysm (AAA), “chimney” endovascular aneurysm repair (ChEVAR), chimney stent graft (CSG), computational fluid dynamics (CFD), hemodynamics, wall shear stress (WSS)

---

## 1. Introduction

Aortic aneurysms (AAs) affect 5–7% of older Americans [1], causing about 15,000 deaths each year, of which 9000 are caused by abdominal aortic aneurysms (AAAs) [1, 2]. Risk of rupture

---

within 1 year for patients with an initial AAA diameter of 5.5–5.9 cm is 9.4% and rises with increase in initial diameter [3]. The most common location of aortic aneurysm formation is the infrarenal section [4].

The traditional method of aneurysm repair is open surgery, in which a large incision in the patient's abdomen facilitates access to the aneurysm site. In recent years, increasingly a number of aneurysms are repaired endovascularly, excluding the aneurysm using stent grafts (SGs) delivered to its site via the arterial system in a minimally invasive procedure. Typically, small incisions in the groin are created in order to provide access to the repair site using the femoral arteries as entry points. Following SG implantation, the aneurysm sac is sealed and blood subsequently flows through the new artificial conduit replacing the previously bulging section of the aorta.

Successful endovascular repair necessitates addressing the specific morphologies of the aneurysm and its surrounding blood vessels. Aneurysms with short proximal (close to the heart) necks account for about 15% of all AAAs [5]. These require the physician performing the procedure to be very accurate when choosing the location of graft deployment. An aneurysm located near a visceral artery ostium is even more challenging to repair endovascularly. Here, the main undertaking is to achieve an adequate seal using the SG while keeping the aortic branches unobstructed [6]. Innovative solutions for this type of predicament include the fenestrated SG (FSG) system. FSGs are custom tailored to the individual morphology of each patient and required months of preparation ahead of the actual procedure [7].

In critical cases where the patient condition does not allow to wait several months for a custom SG system to be manufactured, a novel solution is recently being employed using off-the-shelf SGs. This solution is an endovascular surgical procedure termed the "chimney" technique. In "chimney" endovascular aneurysm repair (ChEVAR), one or more tubular covered stents ("chimneys") are implanted inside the visceral arteries in parallel with the main aortic SG that excludes the aneurysm sac. These covered stents facilitate proper blood flow to arteries that would otherwise be blocked by the main aortic SG. A common case of repair with the "chimney" technique involves proximity of the aneurysm to the two renal arteries (**Figure 1**). In this case, in order to preserve blood flow to the kidneys, a chimney stent graft (CSG) is inserted into each renal artery.

In this study, we investigate the hemodynamics in the abdominal aorta post-ChEVAR and compare it with a healthy abdominal aorta (**Figures 1 and 2**).

Computational fluid dynamics (CFD, ANSYS Fluent package) simulations of pulsatile blood flow during the cardiac cycle are employed. An idealized anatomy of the abdominal aorta is assumed based on averaged measurements taken from cadaver specimens and patient angiograms [8].

The effects CSGs have on abdominal aortic velocity and wall shear stress (WSS) fields are analyzed by evaluating blood flow patterns and regimes.



**Figure 1.** Left: healthy abdominal aorta model. Right: infrarenal aneurysmatic aorta.

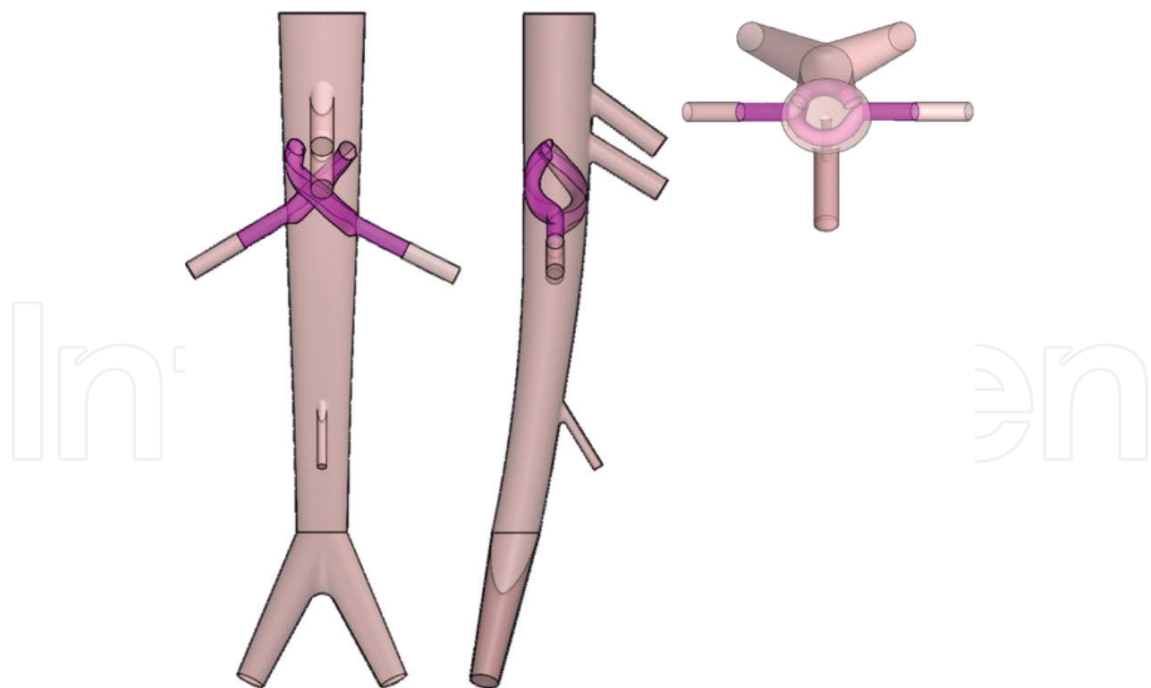


**Figure 2.** Model of the abdominal aorta post-ChEVAR (aneurysm fully replaced by SG). Left to right: front, side, and top views, respectively. Chimney SGs are highlighted pink.

## 2. Methodology

### 2.1. Governing equations

The governing equations for blood flow in the abdominal aorta are the Navier-Stokes Eq. (1) and the continuity Eq. (2) for an incompressible fluid:

$$\rho \frac{\partial v}{\partial t} + \rho(v \cdot \nabla)v - \mu \Delta v + \nabla P = 0 \quad (1)$$

$$\nabla \cdot v = 0 \quad (2)$$

where  $v$ ,  $\rho$ ,  $\mu$ , and  $P$  denote the fluid velocity, density, dynamic viscosity (discussed in detail below), and the pressure field experienced by the fluid, respectively. Blood density is assumed as  $1045 \text{ kg/m}^3$  [9].  $\nabla$ ,  $\nabla \cdot$ , and  $\Delta$  denote the divergence, gradient, and Laplace operators, respectively.

### 2.2. Anatomical model

**Figure 1** presents views of the three-dimensional (3D) model used for analysis of the idealized healthy abdominal aorta. The model is based on angiograms and pressurized cadaver specimens measurements [8]. This model accounts for the elliptical cross section and tapering of the abdominal aorta as it gives off the main arterial branches. It also includes the slight curvature toward the posterior wall. The seven main arterial branches are included: celiac trunk, superior mesenteric artery, left and right renal arteries, inferior mesenteric artery, and the left and right iliac arteries.

The model of the abdominal aorta post-ChEVAR is based on the healthy model. Modifications made account for the renal CSGs. The bulging part of the abdominal aorta is assumed to be completely replaced by the aortic SG and is not included in the analysis. The renal CSG is a covered tubular stent originally used for applications like femoral vascular access. In the "chimney" technique, CSGs are used to ensure blood flow into the renal arteries in cases where standard endovascular aneurysm repair (EVAR) might block the blood flow to these arteries. In this study, the CSGs are modeled as long tube-like structures having smooth inner and outer surfaces. The wall thickness of the CSGs is 0.1 mm, and its free diameter is 15–20% larger than the renal artery diameter. Here, a covered stent with a diameter of 7 mm is used [10, 11]. These dimensions are in compliance with common endograft dimensions in ChEVAR procedures. The three-dimensional shape of the renal CSGs after deployment is helical-like [12], and maintains an outline that does not block any of the major branching arteries.

The deployed CSG is in contact with different components along its length. It is restricted by the renal artery segment and then by the mixed contact area region where the CSG is confined by both the aorta wall and the main aortic SG. Each CSG ends in a segment that protrudes upstream from the aortic SG and into the main aortic duct (10 mm). At each of these segments, the CSG cross section is a little different as it morphs from a circle to a "flattened" elliptical shape and then to a larger circle [13]. These different cross sections are included in the numerical models. The CSG models also incorporate their helical-like nature [12].

Additional assumptions made in the study include rigid (nonflexible) walls, neglecting plaque and thrombus existence, and assuming postdeployment geometry only.

### 2.3. Numerical model

Blood flow behavior in the abdominal aorta along the cardiac cycle is considered to be predominantly laminar [14]. Thus, a laminar CFD solver is employed.

Literature demonstrates that flow characteristics, e.g., WSS, differ by as much as 30% between the distensible and rigid blood vessel models [15]. However, overall flow traits remain similar [16]. Therefore, rigid wall approximation is sufficient for a comparative study. The domain wall boundary conditions have no slip/penetration. The inlet BC is a pulsatile velocity function adapted from a flow rate waveform of an abdominal aorta during rest [17]. This waveform (**Figure 3**) was transformed into a Fourier series and then modified to represent the corresponding average velocity. The spatial distribution of the inlet velocity is approximated as a parabolic profile distributed over the elliptical inlet, and perpendicular to it [15, 18–20]. The seven domain outlets present constant flow ratios with the inlet throughout the cardiac cycle—celiac trunk—21%, superior mesenteric artery—15%, left and right renal arteries—15% each, inferior mesenteric artery—4%, and the left and right iliac arteries—15% each [8]. ANSYS Fluent CFD package is used for the analysis.

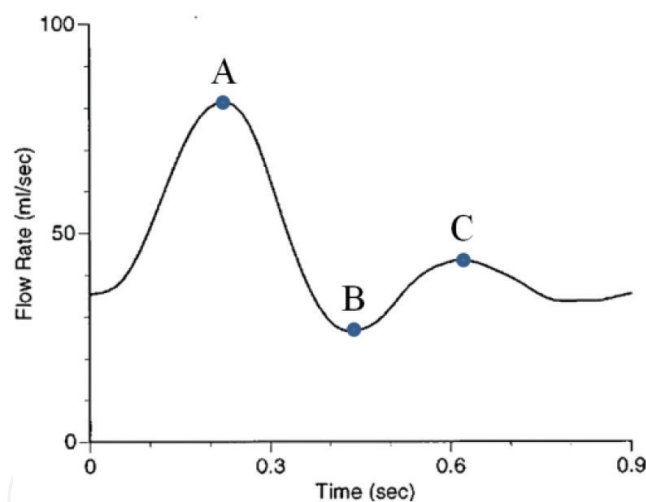


**Figure 3.** Inlet flow rate waveform (representing a single cycle). A: peak systole, B: start of diastole, and C: peak diastole [17].

### 2.4. Numerical discretization

The analysis uses second-order discretization schemes: in space, the least squares cell based for the gradient and the upwind for the momentum and in time the implicit. The spatial domain of the post-ChEVAR abdominal aorta is discretized using 2 million cells (**Figure 4**). Most cells are polyhedral, except prismatic cells used near wall regions to accommodate for the large gradients in these areas. The domain is discretized into tetrahedral elements in the Meshing module of the ANSYS software package and then converted into polyhedral

elements in the Fluent module. The cycle is discretized into 400 time steps. The convergence criterion is a scaled residuals value of  $10^{-4}$ . Periodic convergence is achieved in the third cardiac cycle. The numerical parameters used for the healthy aorta model are similar (Figure 5).

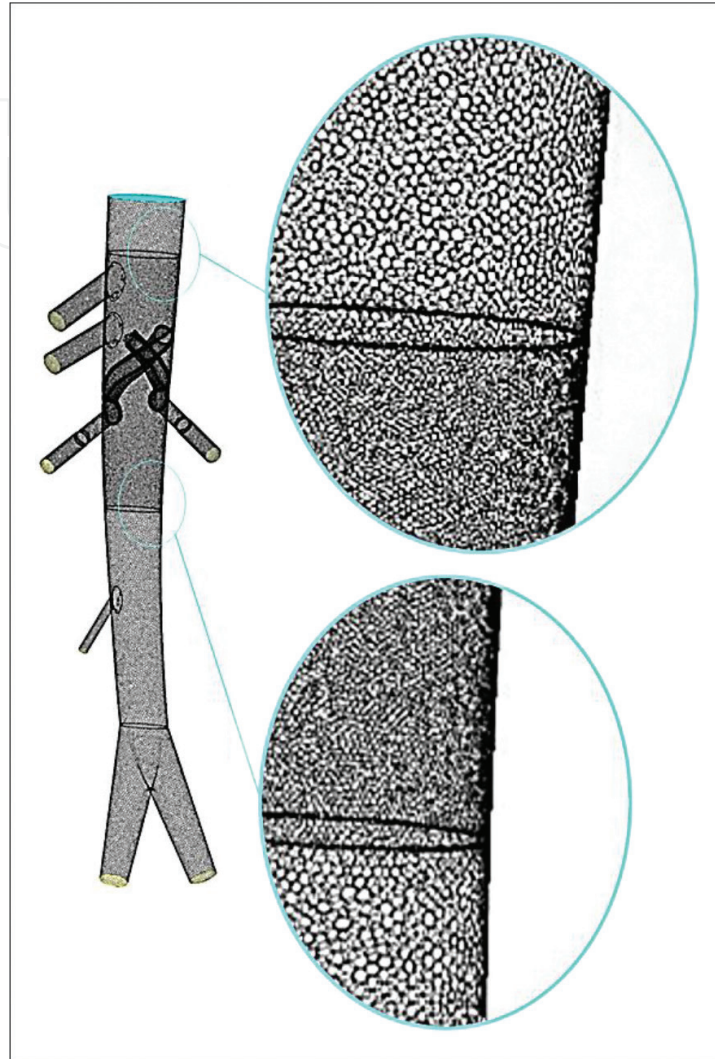


Figure 4. Post-ChEVAR model. Left: angled view. Right: close up of mesh transition zones (light blue ellipses).

## 2.5. Viscosity constitutive model

We studied two viscosity models—the Newtonian approximation and the Carreau constitutive law for shear-thinning fluids [9]. The Newtonian approximation assumes constant blood viscosity while the Carreau model accounts for the strain rate (Table 1):

$$\mu(\gamma) = \mu_{\infty} + (\mu_0 - \mu_{\infty}) (1 + \lambda^2 \gamma^2)^{0.5(n-1)} \quad (3)$$

where  $\gamma$  represents the scalar flow shear rate and  $\mu_s$  and  $\mu_0$  represent the viscosities for infinitely large and zero strain rates, respectively.  $\lambda$  and  $n$  are fluid-specific time constant and power index, respectively (Table 1). The Newtonian viscosity is taken as the viscosity of blood under infinite shear rate, as commonly assumed for blood flow in large arteries such as the aorta [14, 21].

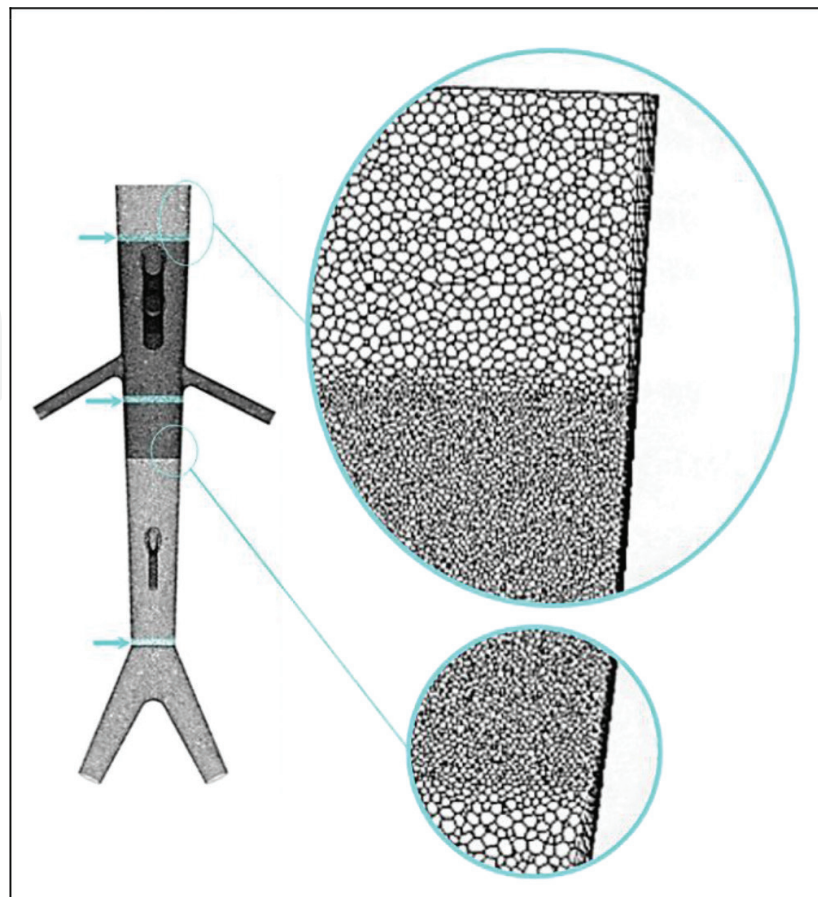


**Figure 5.** Healthy aorta model. Left: wall surfaces evaluated in order to compare the Newtonian and Carreau constitutive models. Top to bottom (in light blue): supra-celiac, infrarenal, and supra-bifurcation cross sections. Right: close up of mesh transition zones (light blue ellipses).

Newtonian viscosity	Carreau viscosity parameters
$\mu = 0.0033 \text{ Pa}\cdot\text{s}$	$\lambda = 1 \text{ s}$
	$n = 0.4$
	$\mu_0 = 0.016 \text{ Pa}\cdot\text{s}$
	$\mu_s = 0.0033 \text{ Pa}\cdot\text{s}$

**Table 1.** Fluid properties for the Newtonian and Carreau blood viscosity models [9].

CFD simulations were performed for the healthy abdominal aorta using both the Newtonian and Carreau viscosity models. Three wall locations were used in order to compare the WSS behaviors of the two models (**Figure 5**). The time-resolved WSSs (axial-Y components) at these locations display different systolic and diastolic peak values (**Figure 6**). The Newtonian model consistently presents peak values lower than the Carreau model at all three locations. Additionally, the systolic phases at the infrarenal height have opposite sign derivatives during  $(0.15-0.25) \cdot t/T$ . The two models generate significantly different mean WSS values—14–20% (**Table 2**). Interestingly, the Carreau model consistently predicts higher absolute value

shear stresses. The flows predicted using the two models also exhibit different patterns. The flow consistently presents more disturbed designs when employing the Newtonian model (Figures 7–9).

Since the discrepancies between the results of both models are not negligible, best practice is to choose the viscosity model that better describes blood behavior—the Carreau model.

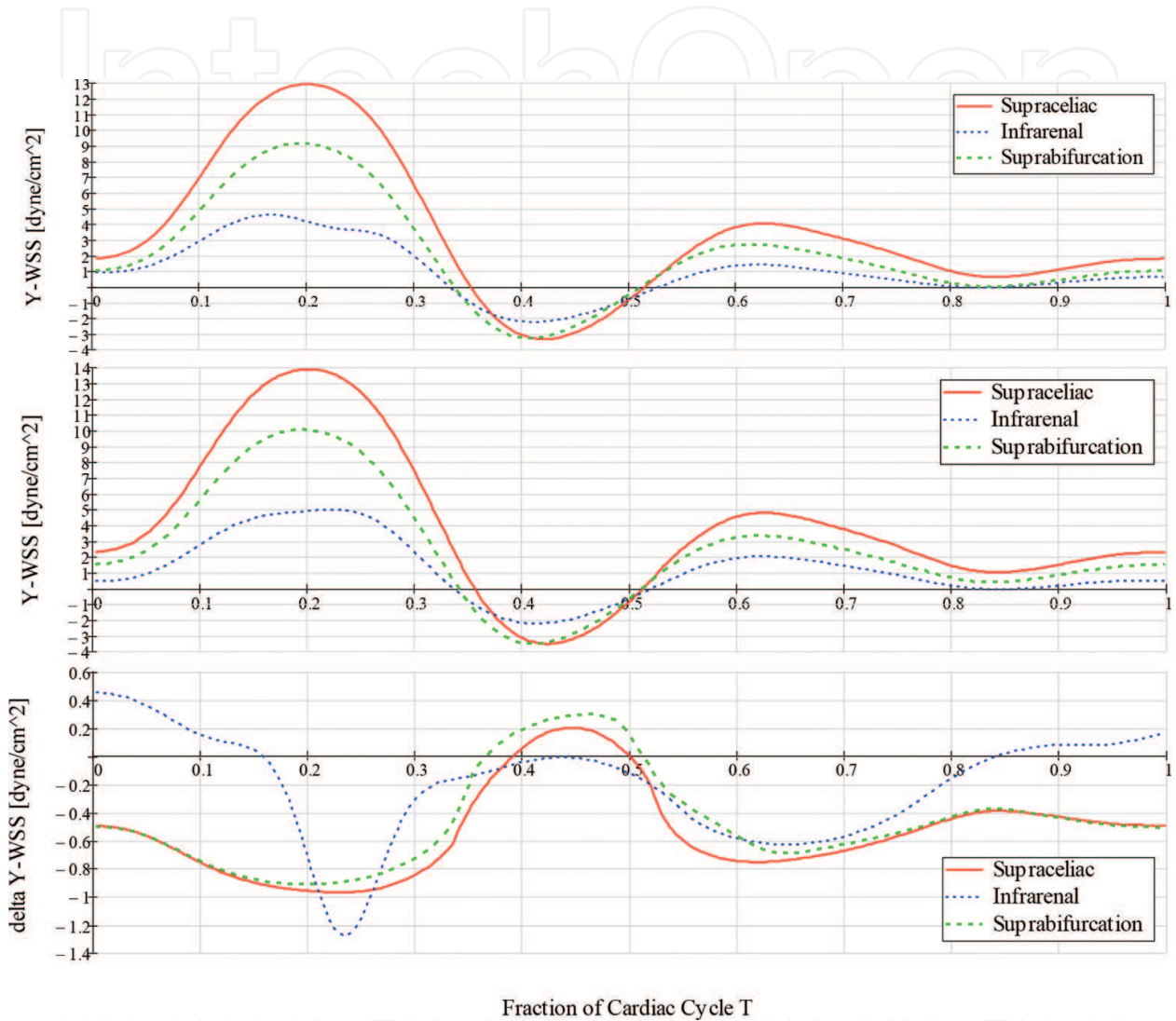
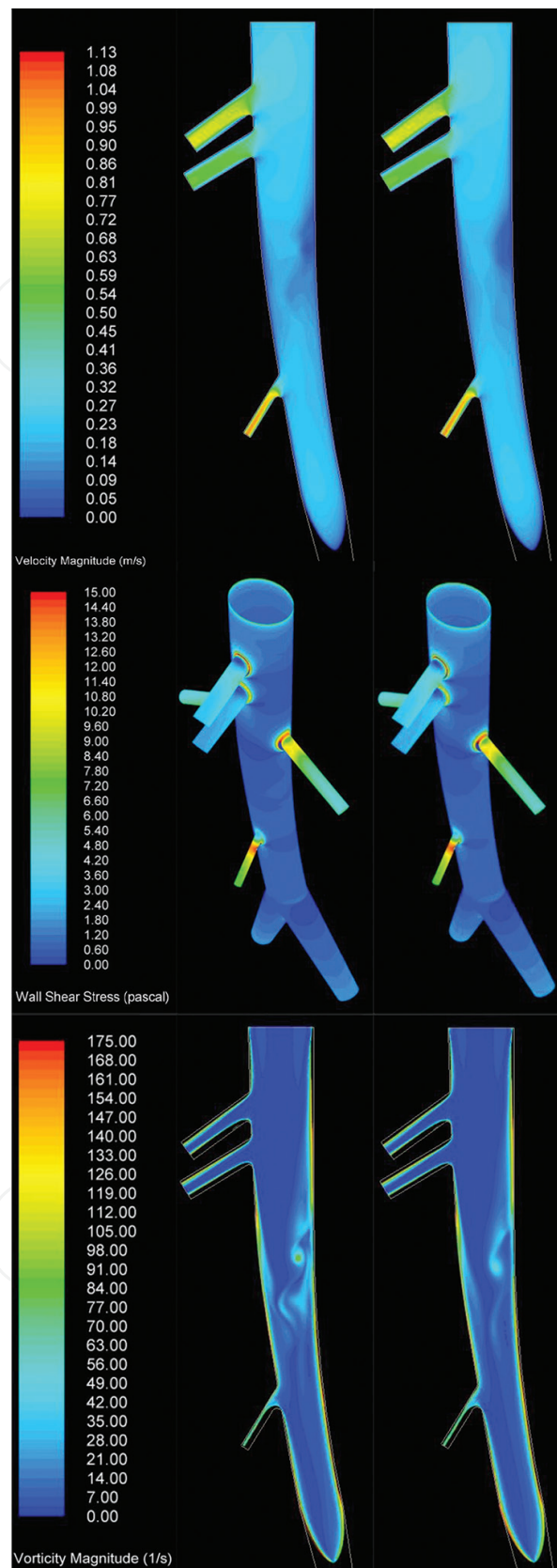


Figure 6. Time-resolved WSS (axial-Y components) curves. Top: Newtonian viscosity model, middle: Carreau viscosity model, bottom: difference between the Newtonian and Carreau models.

WSS (dyne/cm <sup>2</sup> )	Supra-celiac	Infrarenal	Supra-bifurcation
Newtonian	-3.29	-0.888	-1.98
Carreau	-3.832	-1.106	-2.453
Difference (%)	-14	-20	-19

Table 2. Mean WSS (axial component) for the Newtonian and Carreau viscosity models.



**Figure 7.** Contour plots of the hemodynamic conditions at peak systole. Left: Newtonian model. Right: Carreau model. Top row: velocity magnitude. Middle row: WSS magnitude. Bottom row: vorticity magnitude.

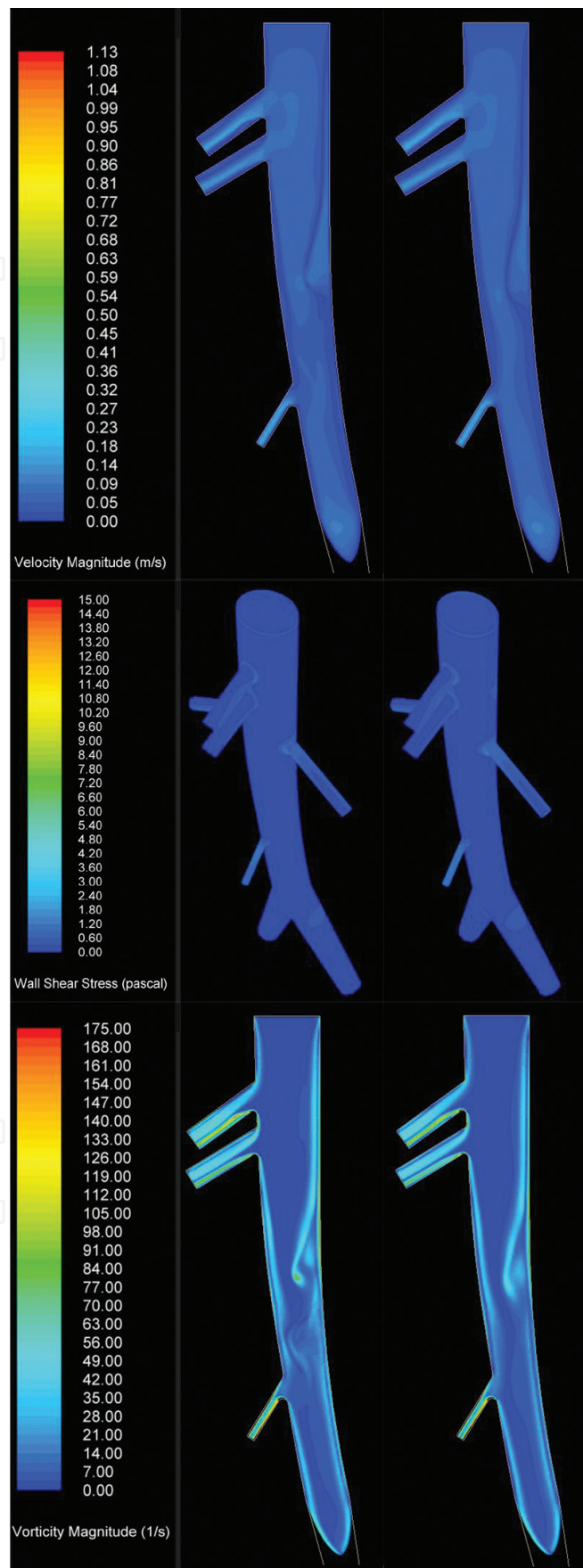


**Figure 8.** Contour plots of the hemodynamic conditions at the start of diastole. Left: Newtonian model. Right: Carreau model. Top row: velocity magnitude. Middle row: WSS magnitude. Bottom row: vorticity magnitude.

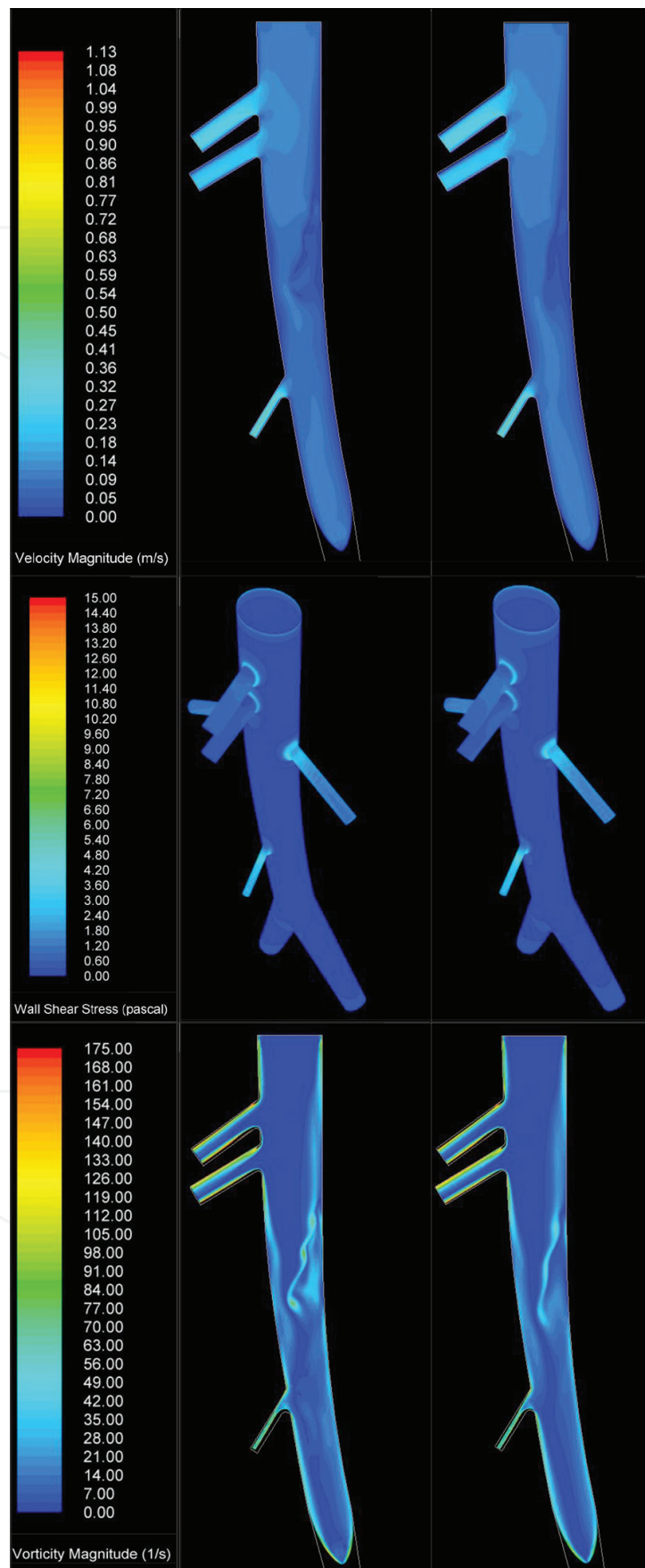


**Figure 9.** Contour plots of the hemodynamic conditions at peak diastole. Left: Newtonian model. Right: Carreau model. Top row: velocity magnitude. Middle row: WSS magnitude. Bottom row: vorticity magnitude.

### 3. Results

#### 3.1. Validation

WSS for the healthy aorta (supra-celiac section) was compared with experimental data available in the literature (Table 3) [22]. The temporal minimum, maximum, and average WSS values of each mesh cell at the supra-celiac ring of Figure 10 were extracted from a full cardiac cycle. The spatial average of each of these parameters along the ring circumference was calculated and tabulated. Pulse WSS is the difference between the maximum and minimum WSSs for each element (also spatially averaged along the circumference). The differences evident in this comparison indicate that the numerical results are in reasonable agreement with the experimental data (Table 3).

WSS (Pa)	Minimum	Maximum	Average	Pulse
Experiment	-0.45	0.87	0.13	1.32
Numerical model	-0.48	0.99	0.19	1.47
Difference (%)	6	14	44	12

Table 3. WSS numerical validation results (axial-Y component), supra-celiac region.

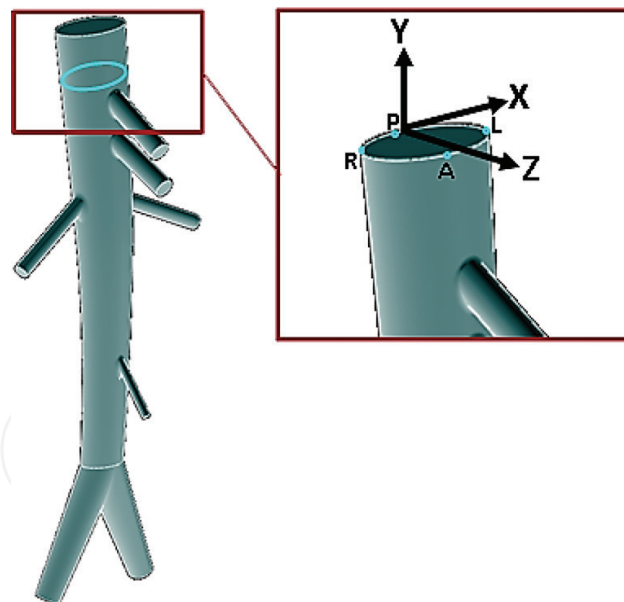
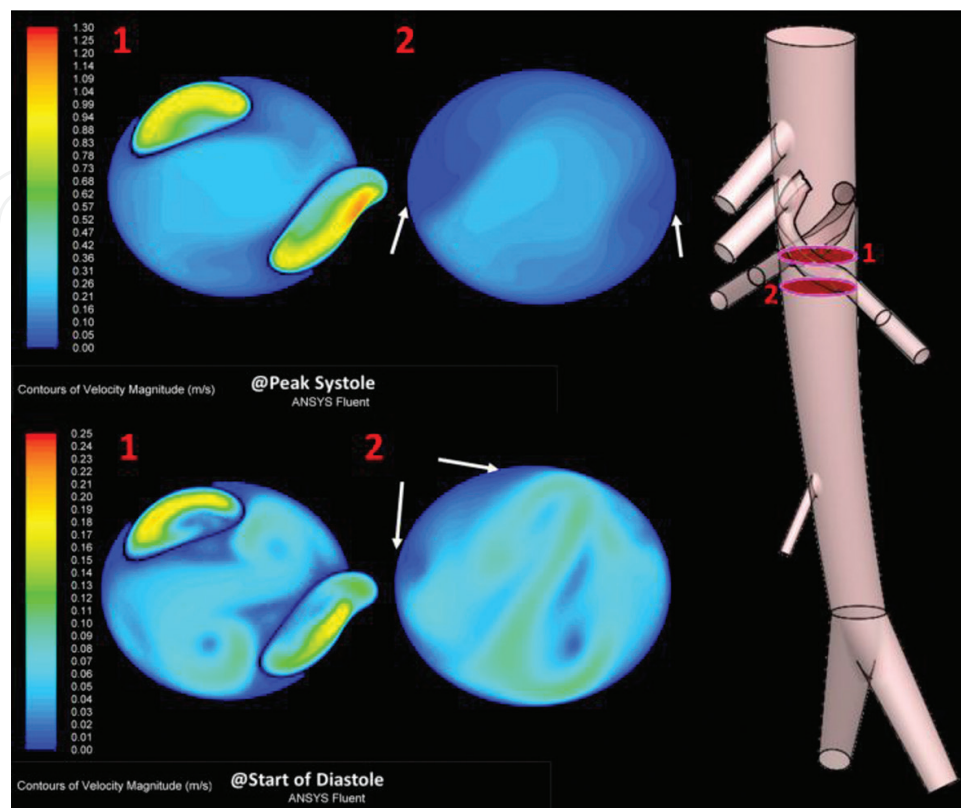


Figure 10. Left: supra-celiac WSS comparison contour (highlighted blue). Right: coordinate system and regions of interest: A— anterior, P— posterior, R—right, L—left.

#### 3.2. Flow patterns

Stagnant regions are formed in the post-ChEVAR aorta downstream from and in close proximity to the CSGs. These regions persist throughout the cardiac cycle, as demonstrated by velocity

contours plotted at the peak of the systole and at the start of the diastole—see **Figures 11** and **12**. These stagnant regions are not present in the healthy model—see **Figures 13** and **14**.



**Figure 11.** Contour plots of blood velocity for the post-ChEVAR model at two horizontal sections below the CSGs (marked red on the right). Top row: peak systole. Bottom row: start of diastole. Arrows: stagnant regions.

The healthy model portrays recirculation and stagnation zones along the infrarenal segment of the posterior wall of the abdominal aortic duct (**Figure 14**). This is evident in the form of closed single-colored patches of low velocity in the **start of the diastole** and the **peak of the diastole**, and less distinctly in the **peak of the systole**. Similar patterns do not appear at this region for the post-ChEVAR model (**Figure 12**).

Several low velocity patches are present downstream from the CSGs for the post-ChEVAR model in the **start of the diastole** and the **peak of the diastole**. In the **start of the diastole**, disorganized streaks and variation in velocity values (contour colors) appear in the renal arteries for the post-ChEVAR model. Stagnation zones radially surround the CSG cross sections for the post-ChEVAR model in all three critical instants A–C of **Figure 3** (**Figures 11** and **12**). In the **peak of the systole** and the **peak of the diastole** the stagnation zones are somewhat elongated in the downstream direction from the CSGs and along the aortic wall.

**Figure 15** displays vector plots of the blood velocity in the beginning of the diastole along the flow direction. The flow patterns for the two models are similar for the section ranging from the inlet and downstream roughly to the location of the celiac trunk and in the segment ranging from the inferior mesenteric artery downstream to the iliac arteries outlets. This holds for

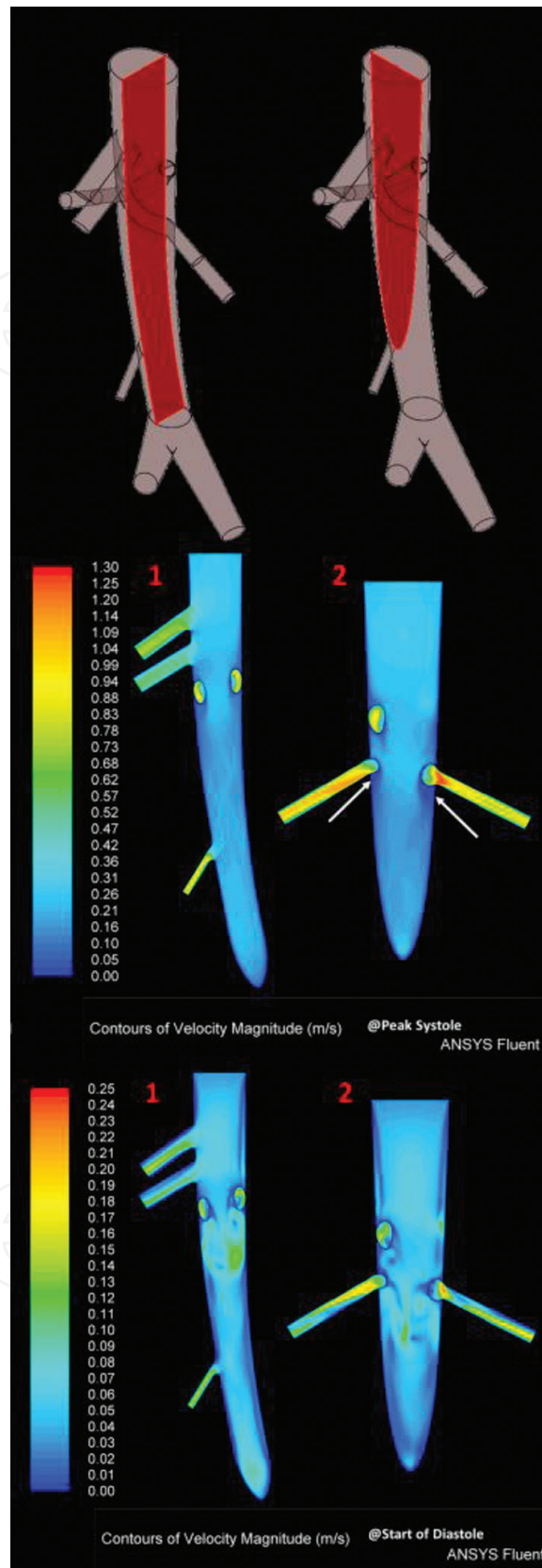


**Figure 12.** Contour plots of blood velocity for the post CheVAR model at two vertical sections (marked red at the top row). Middle row: peak systole. Bottom row: start of diastole.

all three critical instants A–C of **Figure 3**. Several discrepancies are apparent in the middle segment, most notably in the infrarenal region. Here, reverse (retro) flow occurs near the walls in the post-ChEVAR model while in the healthy model these flows take place generally about the centerline (with most flow oriented forward). Additionally, the post-ChEVAR model exhibits somewhat disorganized forward flow in this area while the flow in the healthy model is more structured. Lastly, the velocity profiles along both renal arteries are notably skewed in the post-ChEVAR model compared with the healthy model.

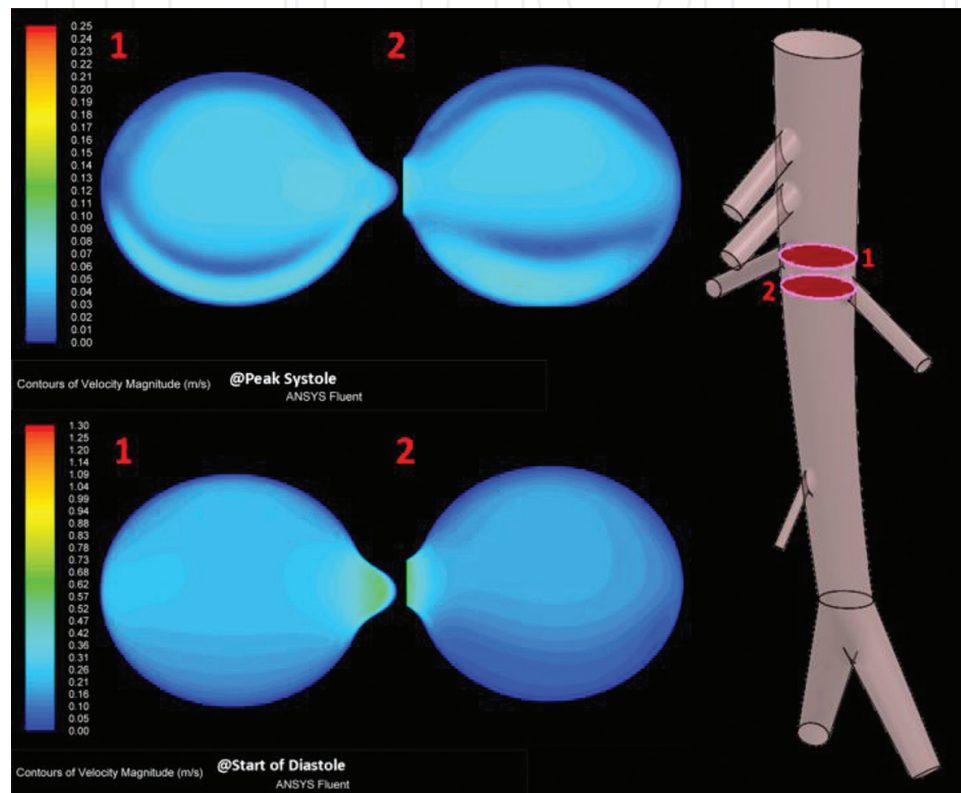


**Figure 13.** Contour plots of blood velocity for the healthy model at two horizontal sections below the CSGs position (marked red on the right, same locations as in **Figure 11**). Top row: peak systole. Bottom row: start of diastole.

**Figure 16** displays contours of the WSS magnitude at the walls for the two models in the three critical instants A–C of **Figure 3**—peak systole, beginning of diastole, and peak diastole. The post-ChEVAR model exhibits low WSS at the CSGs and aortic wall contact zones. Close to these low WSS areas, slightly higher WSS regions in the shape of disorganized patches are present in the peak of the systole and the start of the diastole. Similar regions are present but take the shape of circumferential bands in the peak of the diastole.

For two segments of the aorta, the WSS distributions for the post-ChEVAR model are very similar to those for the healthy model in all three critical instances. These are the segments ranging from the inlet to just downstream of the celiac artery ostium and from roughly mid length between the left renal artery ostium and the inferior mesenteric artery ostium to just downstream of the iliac arteries outlets.

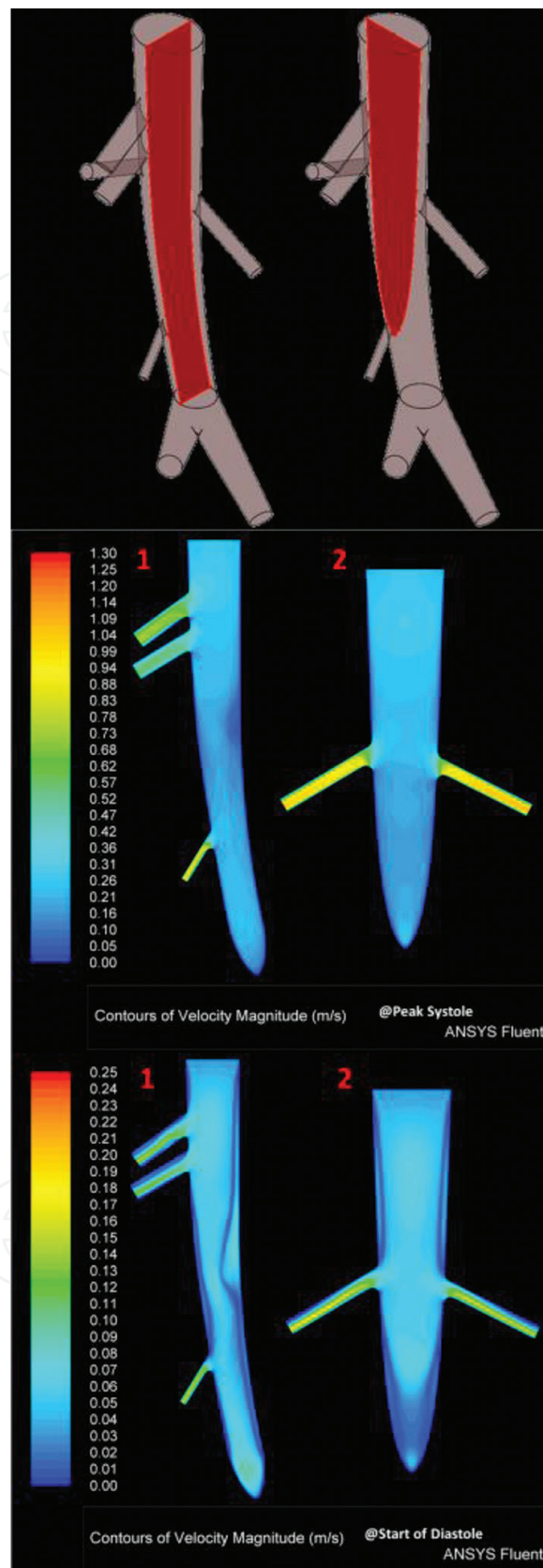


**Figure 14.** Contour plots of blood velocity for the healthy model at two vertical sections (marked red at the top row, same locations as in Figure 12). Middle row: peak systole. Bottom row: start of diastole.

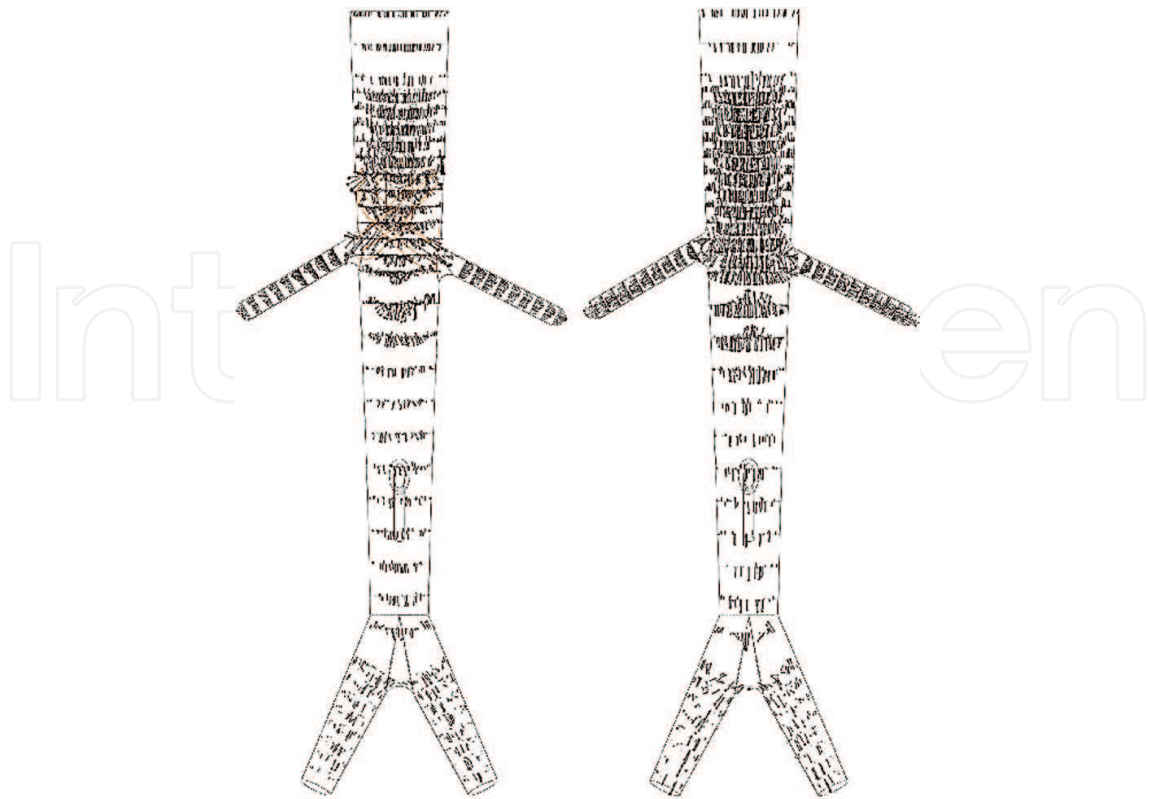


**Figure 15.** Vector plots of blood velocity in the beginning of the diastole. Left: post-CheVAR model. Right: healthy model.

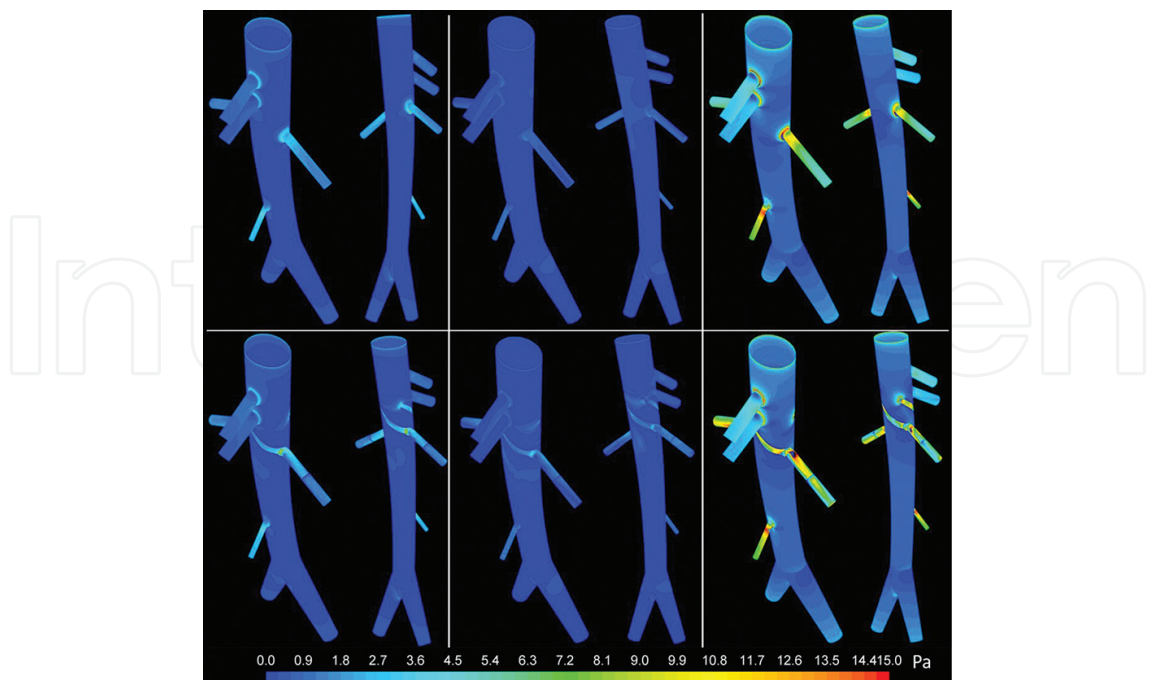


**Figure 16.** Contours of WSS magnitude at the walls—rotated anterior and posterior views. Top row: healthy model. Bottom row: post-CheVAR model. Right to left columns: peak systole, start of diastole, and peak diastole.

### 3.3. Flow regime

**Figure 17** illustrates key locations of interest for which WSSs were evaluated throughout the cardiac cycle. The axial-Y components of these WSSs are plotted along the various sides of the post-ChEVAR aorta (right, left, anterior, and posterior) throughout the cardiac cycle in **Figures 18–20**. **Figure 21** illustrates the axial component of the velocity along the centerline for the post-ChEVAR aorta throughout the cardiac cycle.

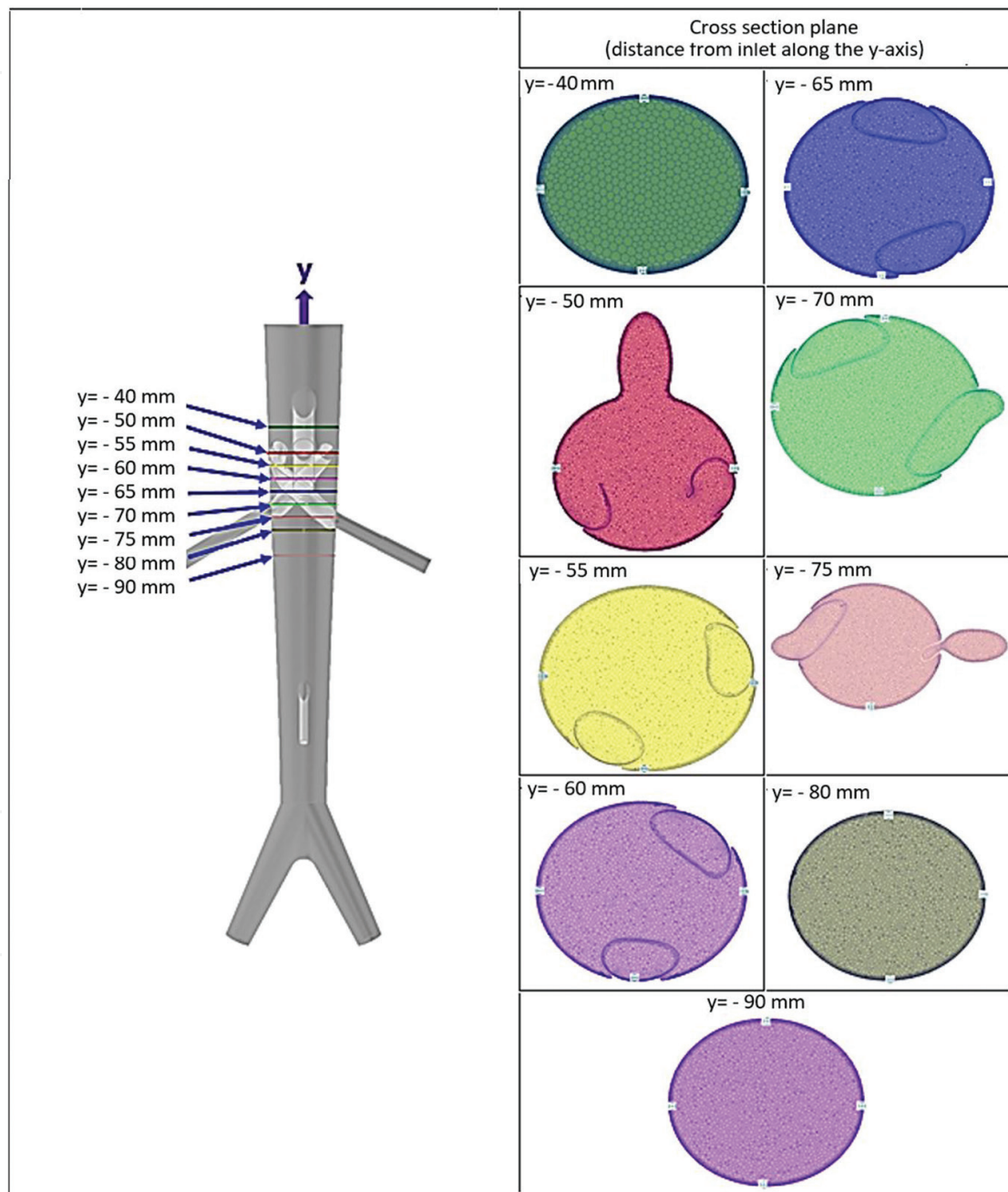


**Figure 17.** The different horizontal planes evaluated for WSSs for the post-ChEVAR model. Left: section planes and their distances from the inlet. Right: the specific points of WSS evaluation at each plane (marked by a dot sign).

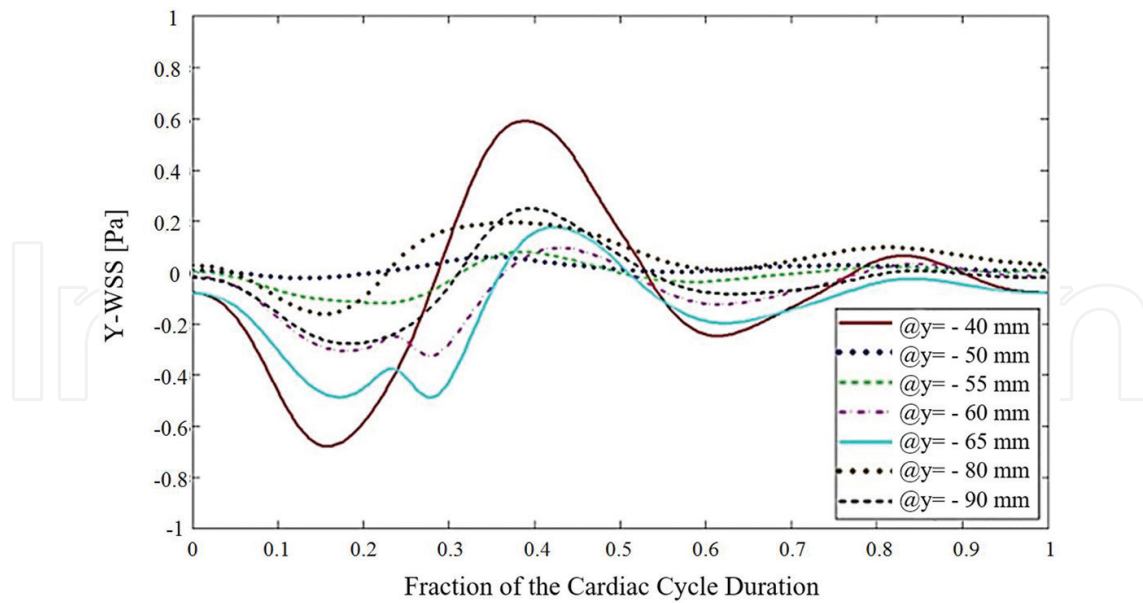


Figure 18. Axial component of the WSS along the right side of the post-ChEVAR aorta throughout the cardiac cycle.

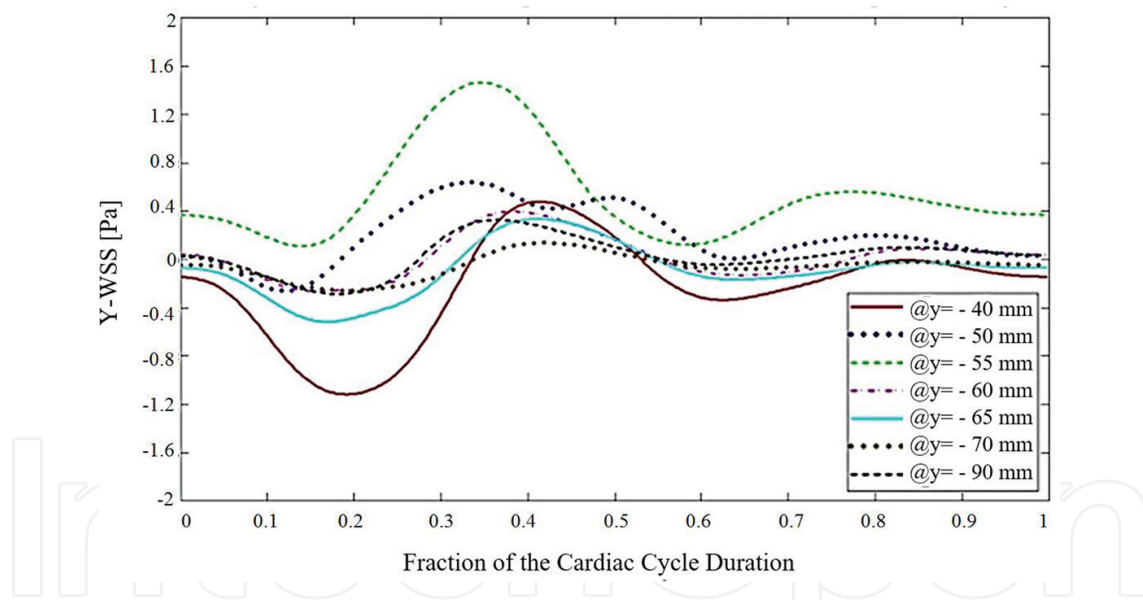
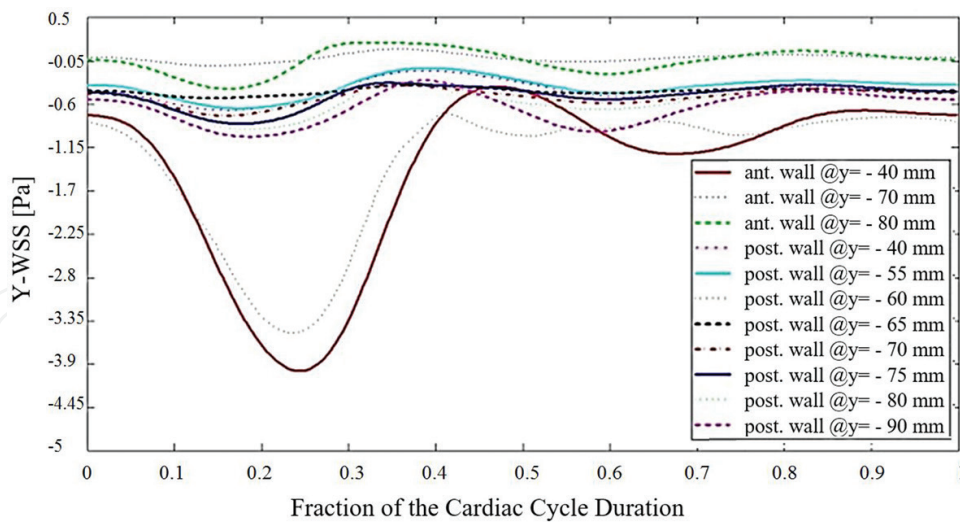
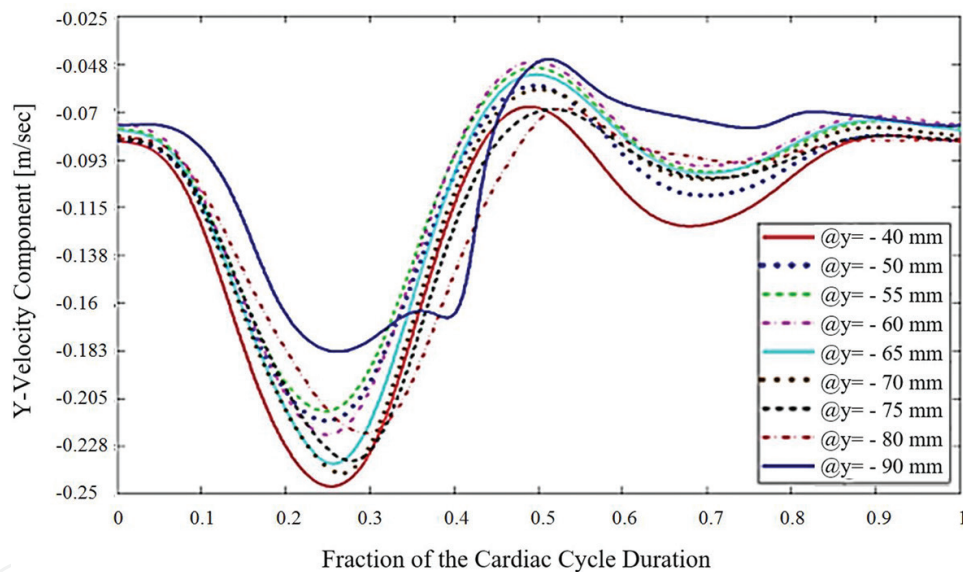


Figure 19. Axial component of the WSS along the left side of the post-ChEVAR aorta throughout the cardiac cycle.

WSSs and velocity patterns follow the inlet flow waveform. There are no high frequency components present. When an inlet flow waveform is free of high frequency components yet locations inside the control volume present velocity/WSS waveforms having high frequency noise, the flow is typically transitional [23]. Here, however, all waveforms are free of high frequency components, thus indicating a laminar flow regime [23]. Therefore, the flow in the post-ChEVAR abdominal aorta is expected to be principally laminar.



**Figure 20.** Axial component of the WSS along the anterior/posterior of the post-CheVAR aorta throughout the cardiac cycle.



**Figure 21.** Axial component of the velocity along the centerline of the post-CheVAR aorta throughout the cardiac cycle.

## 4. Discussion

This study sets out to determine the hemodynamic effects in the abdominal aorta as caused by CSGs placed in the renal arteries (as part of CheVAR repair of infrarenal AAAs). A healthy aorta is employed as a baseline (control) for comparative study. Blood flow in the aorta is mostly adversely affected in the renal arteries region. This is expected since the CSGs constitute a substantial disturbance to the flow that does not exist in healthy abdominal aortas. Their presence induces stagnant velocity regions downstream from the renal arteries throughout the cardiac cycle that might promote thrombosis and inflammation.

Nevertheless, the negative effects of the ChEVAR repair appear relatively mild and are generally localized and confined to the CSGs' vicinity. The velocity fields further downstream for both models are nearly identical. The velocity fields' similarity holds for the upstream segment comprising the inlet as well. **Figure 15**—the vector plots of blood velocity—further supports the overall confined segmental nature of the ChEVAR technique.

The WSS field for the post-ChEVAR model exhibits irregularly shaped patches in the CSGs vicinity (**Figure 16**). In contrast, the WSS field for the healthy model is relatively uniform in this respective region, particularly in the peak of the systole and the beginning of the diastole. Nevertheless, as with the case of the velocity, the WSS fields for the post-ChEVAR model and for the healthy model are very similar downstream from the inferior mesenteric artery and from the inlet to slightly upstream from the CSGs. This again supports the overall confined nature of the ChEVAR technique.

The temporal behavior of the flow field and WSSs for the post-ChEVAR model presents no high frequency oscillations/components and appears to follow the inlet waveform. This indicates lack of turbulent or transitional flow and points toward a predominantly laminar flow regime. Thus, supporting yet again the overall confined nature of the CSG presence.

Overall, we conclude that CSGs are expected to induce localized effects in the hemodynamics of the abdominal aorta, mostly confined to the pararenal segment. This result supports the merit of the ChEVAR technique.

## 5. Conclusions

CSGs presence in the abdominal aorta introduces blood flow and WSSs patterns variations. In particular, the formation of stagnant regions downstream from the CSGs throughout the cardiac cycle, potentially contributing to thrombosis [24]. Nevertheless, in general, the flow field and WSSs appear to remain nearly unaffected in adjacent segments upstream and downstream from the CSGs site. The effects of the CSGs seem to extend about 1 cm upstream and to the approximate location of the inferior mesenteric artery ostium downstream. Furthermore, the CSGs do not appear to shift the flow regime to transitional or turbulent [23]. This suggests that the changes induced by CSGs are limited and confined in their nature, thus supporting the ChEVAR technique merit.

The zone most prone to atherosclerosis, thrombus formation, and other maladies appears to be the infrarenal section of the posterior wall of the abdominal aorta. These diseases are mechanistically linked to low and oscillating WSS [17]. As expected, the post-ChEVAR model is more adversely affected by these phenomena than the healthy model. These results mean that CSGs presence in infrarenal AAAs might function as a minor comorbidity factor in the future health of post-ChEVAR patients.

Our findings are in good agreement with data indicating a relatively high success rate for ChEVAR procedures performed in recent years, evident both in short- and long-term patient follow ups [25].

## Author details

Hila Ben Gur<sup>1</sup>, Moses Brand<sup>2\*</sup>, Gábor Kósa<sup>1</sup> and Saar Golan<sup>2,3</sup>

\*Address all correspondence to: mosheb@ariel.ac.il

1 School of Mechanical Engineering, Faculty of Engineering, Tel Aviv University, Tel Aviv, Israel

2 Department of Mechanical Engineering & Mechatronics, Faculty of Engineering, Ariel University, Ariel, Israel

3 Department of Chemical Engineering, Faculty of Engineering, Ariel University, Ariel, Israel

## References

- [1] A. S. Les, S. C. Shadden, C. A. Figueroa, J. M. Park, M. M. Tedesco, R. J. Herfkens, R. L. Dalman, and C. A. Taylor, "Quantification of hemodynamics in abdominal aortic aneurysms during rest and exercise using magnetic resonance imaging and computational fluid dynamics," *Ann. Biomed. Eng.*, vol. 38, no. 4, pp. 1288–1313, 2010.
- [2] C. Fleming, E. P. Whitlock, T. L. Beil, and F. A. Lederle, "Screening for abdominal aortic aneurysm: a best-evidence systematic review for the U.S. preventive services task force," *Ann. Intern. Med.*, vol. 142, no. 3, pp. 203–213, 2005.
- [3] F. A. Lederle, G. R. Johnson, S. E. Wilson, D. J. Ballard, W. D. Jordan, J. Blebea, F. N. Littooy, J. A. Freischlag, D. Bandyk, J. H. Rapp, and A. A. Salam, "Rupture rate of large abdominal aortic aneurysms in patients refusing or unfit for elective repair," *JAMA*, vol. 287, no. 22, pp. 2968–2972, 2002.
- [4] D.C. Guo, C. L. Papke, R. He, and D. M. Milewicz, "Pathogenesis of thoracic and abdominal aortic aneurysms," *Ann. N. Y. Acad. Sci.*, vol. 1085, pp. 339–52, Nov. 2006.
- [5] Y. Li, Z. Hu, C. Bai, J. Liu, T. Zhang, Y. Ge, S. Luan, and W. Guo, "Fenestrated and chimney technique for juxtarenal aortic aneurysm: a systematic review and pooled data analysis," *Sci. Rep.*, vol. 6, no. February, p. 20497, 2016.
- [6] M. Brand, I. Avrahami, A. Nardi, D. Silverberg, and M. Halak, "Clinical, hemodynamical and mechanical aspects of aortic aneurysms and endovascular repair," in *Aortic Aneurysms: Risk Factors, Diagnosis, Surgery and Repair*, F. Daniel and F. Hatig, Eds. New York: Nova Science Publishers Inc., 2013, pp. 181–192.
- [7] I. Avrahami, M. Brand, T. Meirson, Z. Ovadia-Blechman, and M. Halak, "Hemodynamic and mechanical aspects of fenestrated endografts for treatment of Abdominal Aortic Aneurysm," *Eur. J. Mech. – B/Fluids*, vol. 35, pp. 85–91, 2012.
- [8] J. E. Moore, D. N. Ku, C. K. Zarins, and S. Glagov, "Pulsatile flow visualization in the abdominal aorta under differing physiologic conditions: implications for increased susceptibility to atherosclerosis," *J. Biomech. Eng.*, vol. 114, pp. 391–397, 1992.

- [9] B. Ene-Iordache, L. Mosconi, G. Remuzzi, and A. Remuzzi, "Computational fluid dynamics of a vascular access case for hemodialysis.," *J. Biomech. Eng.*, vol. 123, no. 3, pp. 284–292, 2001.
- [10] F. Pecoraro, T. Pfammatter, M. Lachat, D. Mayer, Z. Rancic, M. Glenck, G. Puipe, and F. J. Veith, "Limitations to EVAR with chimney and periscope grafts," *Endovasc. Today*, no. February, pp. 56–62, 2014.
- [11] G. Mestres, J. P. Uribe, C. García-Madrid, E. Miret, X. Alomar, M. Burrell, and V. Riambau, "The best conditions for parallel stenting during EVAR: an in vitro study.," *Eur. J. Vasc. Endovasc. Surg.*, vol. 44, no. 5, pp. 468–473, Nov. 2012.
- [12] R. Coscas, H. Kobeiter, P. Desgranges, and J.P. Becquemin, "Technical aspects, current indications, and results of chimney grafts for juxtarenal aortic aneurysms.," *J. Vasc. Surg.*, vol. 53, no. 6, pp. 1520–1527, 2011.
- [13] J. L. de Bruin, K. K. Yeung, W. W. Niepoth, R. J. Lely, Q. Cheung, A. de Vries, and J. D. Blankensteijn, "Geometric study of various chimney graft configurations in an in vitro juxtarenal aneurysm model.," *J. Endovasc. Ther.*, vol. 20, no. 2, pp. 184–190, 2013.
- [14] L. Morris, P. Delassus, M. Walsh, and T. McGloughlin, "A mathematical model to predict the in vivo pulsatile drag forces acting on bifurcated stent grafts used in endovascular treatment of abdominal aortic aneurysms (AAA).," *J. Biomech.*, vol. 37, no. 7, pp. 1087–1095, 2004.
- [15] T. Shipkowitz, V. G. J. Rodgers, L. J. Frazin, and K. B. Chandran, "Numerical study on the effect of steady axial flow development in the human aorta on local shear stresses in abdominal aortic branches," *J. Biomech.*, vol. 31, pp. 995–1007, 1998.
- [16] G. M. H. and F. F. M. M. H. Friedman, C. B. Barger, D. D. Duncan, "Effects of arterial compliance and non-Newtonian rheology on correlations between intimal thickness and wall shear," *J. Biomech. Eng.*, vol. 114, no. 3, p. 317, 1992.
- [17] C. A. Taylor, T. J. R. Hughes, and C. K. Zarins, "Finite element modeling of three-dimensional pulsatile flow in the abdominal aorta: relevance to atherosclerosis," *Ann. Biomed. Eng.*, vol. 26, pp. 975–987, 1998.
- [18] B. T. Tang, C. P. Cheng, M. T. Draney, N. M. Wilson, P. S. Tsao, R. J. Herfkens, and C. A. Taylor, "Abdominal aortic hemodynamics in young healthy adults at rest and during lower limb exercise: quantification using image-based computer modeling.," *Am. J. Physiol. Heart Circ. Physiol.*, vol. 291, no. 2, pp. H668–H676, 2006.
- [19] C. P. Cheng, R. J. Herfkens, and C. A. Taylor, "Abdominal aortic hemodynamic conditions in healthy subjects aged 50-70 at rest and during lower limb exercise: in vivo quantification using MRI," *Atherosclerosis*, vol. 168, no. 2, pp. 323–331, 2003.
- [20] R. A. Jamison, G. J. Sheard, A. Fouras, and K. Ryan, "The validity of axisymmetric assumptions when investigating pulsatile biological flows," *Austral. Math. Soc.*, vol. 50, pp. 713–728, 2009.
- [21] P. Tazraei, A. Riasi, and B. Takabi, "The influence of the non-Newtonian properties of blood on blood-hammer through the posterior cerebral artery," *Math. Biosci.*, vol. 264, no. 1, pp. 119–127, 2015.

- [22] J. E. Moore, S. Glagov, and D. N. Ku, "Fluid wall shear stress measurements in a model of the human abdominal aorta: oscillatory behavior and relationship to atherosclerosis," *Atherosclerosis*, vol. 9150, pp. 225–240, 1994.
- [23] M. Bozzetto, B. Ene-Iordache, and A. Remuzzi, "Transitional flow in the venous side of patient-specific arteriovenous fistulae for hemodialysis," *Ann. Biomed. Eng.*, vol. 44, no. 8, pp. 2388–2401, 2016.
- [24] D. N. Ku, "Blood flow in arteries," *Annu. Rev. Fluid Mech.*, vol. 29, no. 1, pp. 399–434, 1997.
- [25] Y. Li, T. Zhang, W. Guo, C. Duan, R. Wei, Y. Ge, X. Jia, and X. Liu, "Endovascular chimney technique for juxtarenal abdominal aortic aneurysm: a systematic review using pooled analysis and meta-analysis," *Ann. Vasc. Surg.*, vol. 29, no. 6, pp. 1141–1150, 2015.